



## Full Length Article

# More than the barrier effect: Biodegradable Mg-Ag alloy membranes for guided bone/tissue regeneration

Sihui Ouyang<sup>a,b,c</sup>, Xiong Wu<sup>a</sup>, Li Meng<sup>d</sup>, Xuerui Jing<sup>a</sup>, Liying Qiao<sup>a,b,c</sup>, Jia She<sup>a,b,c,\*</sup>, Kai Zheng<sup>d,\*</sup>, Xianhua Chen<sup>a,b,c</sup>, Fusheng Pan<sup>a,b,c</sup>

<sup>a</sup>College of Materials Science and Engineering, Chongqing University, Chongqing 400044, China

<sup>b</sup>National Engineering Research Center for Magnesium Alloys, Chongqing University, Chongqing 400044, China

<sup>c</sup>National Key Laboratory of Advanced Casting Technologies, Chongqing University, Chongqing, 400044, China

<sup>d</sup>Jiangsu Key Laboratory of Oral Diseases & Jiangsu Province Engineering Research Center of Stomatological Translational Medicine, Nanjing Medical University, Nanjing 210029, China

Received 2 January 2024; received in revised form 23 March 2024; accepted 25 March 2024

Available online xxx

## Abstract

Magnesium (Mg) and its alloys have emerged as promising candidates for guided bone/tissue regeneration (GBR/GTR) due to their good mechanical properties, biosafety, and biodegradability. In this study, we present a pioneering application of Mg-Ag alloys featuring tunable corrosion behaviors for GBR/GTR membranes, showcasing their in vitro antibacterial effects, cell migration, and osteogenic differentiation abilities. Mg-Ag alloys with different Ag contents were engineered to facilitate the cell migration of murine fibroblasts (L929) and the osteogenic differentiation of rat bone mesenchymal stem cells (rBMSCs). The Mg-Ag alloy consisted of recrystallized  $\alpha$ -Mg grains and fine Mg<sub>4</sub>Ag second phases, with an observable refinement in the average grain size to 5.6  $\mu$ m with increasing Ag content. Among the alloys, Mg-9Ag exhibited optimal mechanical strength and moderate plasticity (tensile yield strength of 205.7 MPa, elongation of 20.3%, and a maximum bending load of 437.2 N). Furthermore, the alloying of Ag accelerated the cathodic reaction of pure Mg, leading to a slightly increased corrosion rate of the Mg-Ag alloys while maintaining acceptable general corrosion. Notably, compared with pure Mg, Mg-Ag alloys had superior antibacterial effects against *Porphyromonas gingivalis* (*P. gingivalis*) and *Staphylococcus aureus* (*S. aureus*). Taken together, these results provide evidence for the significant clinical potential of Mg-Ag alloys as GBR/GTR membranes.

© 2024 Chongqing University. Publishing services provided by Elsevier B.V. on behalf of KeAi Communications Co. Ltd.

This is an open access article under the CC BY-NC-ND license (<http://creativecommons.org/licenses/by-nc-nd/4.0/>)

Peer review under responsibility of Chongqing University

**Keywords:** Biodegradable; Magnesium alloy; Antibacterial; Guided tissue regeneration; Guided bone regeneration.

## 1. Introduction

Guided bone/tissue regeneration (GBR/GTR) technology is considered as one of the most effective treatments that can promote periodontal defect regeneration [1–3]. It works by placing a structural membrane like a barrier between the gingival tissue and the periodontal bone defect, originally targeted at providing mechanical support to prevent fibroblasts or epithelial cells from growing into the bone defect area [4].

Although specific clinical reports have documented adequate periodontal tissue regeneration with the GBR/GTR strategy, complications, notably the elevated risk of post-operative infection and the high incidence of wound dehiscence, have proven unsatisfactory [5,6]. This discouraging outcome can be attributed to the limited properties of traditional membranes serving solely as physical barriers without essential osteogenic and antibacterial abilities crucial for promoting the repair of damaged periodontal tissue. Commercial non-absorbable membranes, such as polytetrafluoroethylene (PTFE) and titanium (Ti), boast excellent mechanical properties [7,8]. However, their bioinert nature necessitates secondary surgical removal. On the other hand, absorbable

\* Corresponding authors.

E-mail addresses: [jiash@foxmail.com](mailto:jiash@foxmail.com) (J. She), [kaizheng@njmu.edu.cn](mailto:kaizheng@njmu.edu.cn) (K. Zheng).

<https://doi.org/10.1016/j.jma.2024.03.022>

2213-9567/© 2024 Chongqing University. Publishing services provided by Elsevier B.V. on behalf of KeAi Communications Co. Ltd. This is an open access article under the CC BY-NC-ND license (<http://creativecommons.org/licenses/by-nc-nd/4.0/>) Peer review under responsibility of Chongqing University

membranes, like collagen, offer advantages in terms of biocompatibility and cell affinity [9]. Nevertheless, their unpredictable degradation rates and insufficient strength pose challenges [10]. Crucially, the implantation of these barrier membranes creates open wounds vulnerable to penetration by the abundant bacteria within the oral cavity [11]. Therefore, an ideal GBR/GTR membrane should encompass the following attributes: sufficient mechanical properties, appropriate degradability, biocompatibility, outstanding antibacterial effects, and the capacity to facilitate both wound healing and osteogenesis [12–14].

Pure Mg has been demonstrated efficacy as a barrier membrane, offering sufficient mechanical properties, and its corrosion-induced local alkaline environment exhibits an antibacterial effect [15,16]. Nevertheless, the dynamic environment within the human body significantly diminishes its antibacterial effect [17]. The introduction of alloying elements is a good option to optimize the properties of Mg alloys by customizing the formability, mechanical performance and biological functionality [18]. Silver (Ag) exhibits stable broad-spectrum antibacterial activity, and has been used to treat chronic wound dehiscence [19]. Furthermore, considering the oligodynamic antibacterial capability of Ag at a relatively low concentration, Mg-Ag alloys with antibacterial properties have garnered significant attention [20]. Bryła et al. [21] investigated the corrosion behavior of the Mg-Ag alloy in simulated body fluids (SBF), both in its as-cast state and after equal-channel angular pressing. The findings revealed that grain refinement had a minimal impact on the corrosion rate of the Mg-Ag alloy. Liu et al. [22] optimized the distribution of second phases in as-cast Mg-Ag alloys through heat treatment to enhance their corrosion resistance. The antibacterial effects of Mg-Ag alloys against *Staphylococcus* strains are highly dependent on the Ag content. Furthermore, Chen et al. [23] discovered that, in comparison with Mg-Ca alloy, Mg-Ca-Zn-Ag alloy exhibited superior antibacterial and osteogenic properties. Notably, when the Ag content was 1.5 wt.%, the Mg alloy demonstrated significantly enhanced osteogenic activity and bone substitution rate following implantation in rat femoral defects. This enhancement can be attributed to the additional release of  $Zn^{2+}$  and  $Ag^+$  ions, which stimulate an extensive bone remodeling process. Herein, we hypothesized that Mg-Ag alloys, featuring tunable corrosion behaviors as GBR/GTR membranes, could promote wound healing, osteogenic differentiation and prevent bacterial invasion.

In the present study, biodegradable Mg-Ag alloys were tailored by introducing varying Ag contents for GBR/GTR membranes. The microstructure evolution and mechanical properties of Mg-Ag alloys were clarified. The distribution of second phases, corrosion behavior and  $Ag^+$  release kinetics of Mg-Ag alloys have been investigated systematically. To realize the bio-functionality of Mg-Ag alloy membranes, special attention was paid to their antibacterial activity against *Porphyromonas gingivalis* (*P. gingivalis*) and *Staphylococcus aureus* (*S. aureus*). Furthermore, the cytotoxicity, cell migration and osteogenic differentiation of Mg-Ag alloys were evaluated from the perspective of GBR/GTR membrane application.

## 2. Materials and methods

### 2.1. Samples preparation

Pure Magnesium ( $\geq 99.95$  wt.%) and silver granules (99.99 wt.%) were used to prepare Mg-Ag alloy ingots, which were melted in a stainless-steel crucible at 720 °C, with the protect atmosphere of  $CO_2$  and  $SF_6$ . All the Mg alloy ingots were machined into the billets with a diameter of 80 mm, and hot extruded at 350 °C, with the extrusion ratio of 25:1. The obtained Mg alloy rods have the nominal compositions of pure Mg (denoted Mg), Mg-5 wt.%Ag (denoted Mg-5Ag) and Mg-9 wt.%Ag (denoted Mg-9Ag). Mg alloy membranes, with a thickness of 1 mm, were cut along the extrusion direction of the obtained Mg alloy rods, and polished in 5% (v/v) nitric acid ethanol solution.

### 2.2. Microstructure characterization

The grain size, orientation and texture of Mg alloy membranes were analyzed by Electron Backscatter Diffraction (EBSD) performed by a field emission scanning electron microscopy (JEOL JSM-7800F), equipped with HKL Chanel 5 System. The phase compositions were characterized through the X-ray diffractometer (XRD, D/Max 2500 PC).

### 2.3. Mechanical properties

The tensile samples have a gauge length of 9 mm, a width of 4 mm, and a thickness of 1 mm, and the tensile test was conducted with a strain rate of  $0.001\ s^{-1}$ . To character the shaping ability of Mg alloy membranes, three-point bending tests were performing by using a Universal testing machine (MTS EDT503A Series). The samples were machined into 30 mm (ED)  $\times$  12 mm (TD)  $\times$  1 mm, and placed on two support rollers with the distance of  $13\pm 0.5$  mm. The loading rate is set as 1 mm/min, and all the tests were repeated 5 times.

### 2.4. Immersion test

The square Mg sample with a size of  $10 \times 10\ mm^2$ , and a thickness of 1 mm was soaked in Dulbecco's Modified Eagle Medium (DMEM) at 37 °C with shaking at a rate of 90 rpm. The ratio of solution volume to the surface area of samples is  $20\ mL\cdot cm^{-2}$ . The detailed composition of DMEM can be found in Ref [24]. The Mg alloy sample utilized for the weight loss test has a diameter of 1 mm. After sealing the back and surrounding sides with epoxy resin, it was soaked for 72 h. Subsequently, the sample was immersed in a dilute chromic acid aqueous solution ( $180\ g\cdot L^{-1}$ ) for 5 min to eliminate corrosion products. Repeat the cleaning process multiple times for each sample until no significant difference in mass loss is discerned between two consecutive cleanings. The average corrosion rate was calculated based on the weight loss rate ( $\Delta W$ ) by using the following equation [25]:

$$V_{\Delta W}(\text{mm}\cdot\text{y}^{-1}) = 2.10\Delta W(\text{mg}\cdot\text{cm}^{-2}\cdot\text{d}^{-1})$$

The pH values and the concentration of released  $\text{Ag}^+$  were recorded at different intervals by ICP-MS (NexION 5000, PerkinElmer). ATR-FTIR spectroscopy (Nicolet iS5, Thermo Fisher Scientific) from 4000 to  $400\text{ cm}^{-1}$  was also conducted to identify the functional groups of the corroded samples. X-ray photoelectron spectrometer (XPS, ESCALAB 250Xi system, Thermo Fisher Scientific) with  $\text{Al K}\alpha$  X-ray source was also utilized to identify the surface chemistry of the corrosion products.

## 2.5. Electrochemical test

To conduct electrochemical tests in DMEM, employ Mg alloy samples with a diameter of 1 mm, thereby exposing a surface area of  $0.785\text{ cm}^2$  to the DMEM. The open circuit potential evolution, electrochemical impedance spectroscopy (EIS) and potentiodynamic polarization (PDP) using Gamry Interface 1010E. A three-electrode cell with Mg alloys as the working electrode, the saturated calomel electrode as the reference electrode and platinum electrode as the counter electrode were used. A scanning rate of  $1\text{ mV}\cdot\text{s}^{-1}$  was used in the PDP test, and the frequency range from  $10^{-2}$  Hz to  $10^5$  Hz was applied in EIS tests. The EIS spectra were fitted with the ZSimpWin software. The polarization resistance ( $R_p$ ) and corrosion current density ( $I_{\text{corr}}$ ) were estimated with the Stern-Geary equation [26].

## 2.6. In vitro cell evaluation

### 2.6.1. Cell cytotoxicity assay

Murine fibroblasts (L929) were used to assess in vitro cytotoxicity. According to ISO10993-12:2021 standard, extracts of Mg and Mg-Ag alloys were prepared by soaking in DMEM at  $37^\circ\text{C}$  for 72 h under humidified 5%  $\text{CO}_2$  atmosphere, and the ratio of the surface area of samples to the volume of the medium was  $3\text{ cm}^2/\text{mL}$  [27]. The cytotoxicity was evaluated by an indirect method from the extracts supplemented with 10% fetal bovine serum (FBS, Vivacell), 1% penicillin/streptomycin (PS, NCM Biotech). L929 cells were seeded at a density of  $4 \times 10^4$  cells/ $\text{cm}^2$  and the culture medium without extracts was used as negative control. After incubation for 1 d, the medium with 10% Cell Counting Kit-8 (CCK-8; Dojindo Kagaku Co) reagent was added to each well, and incubated at  $37^\circ\text{C}$  for 2 h, then the optical density (OD) was recorded at 450 nm with a microplate reader.

### 2.6.2. Cell migration assay

The cell migration capacity of L929 cells cultured in 10% concentration extracts of Mg alloy membranes, both scratch and transwell migration assays were applied. L929 cells were seeded in 6-well plates. Cells on the plate with 90% confluency were scratched by using a P200 pipette tip, and then rinsed twice to remove detached cells. The Mg extracts were added to the well and cultured for 24 h. The photo of each group was taken after 0 h and 24 h of incubation under a Leica DMIRE 2 microscope. The wound contraction among

groups was calculated according to the following formula:

$$\text{Wound contraction} = \frac{W_{d0} - W_{dt}}{W_{d0}} \times 100\%$$

$W_{d0}$  and  $W_{dt}$  are the wound area recorded at 0 h and 24 h, respectively.

L929 cells were seeded in the upper chamber (Millipore) of 12 well plates, while 600  $\mu\text{L}$  of extracts were added to the lower chamber. After 48 h of incubation, the upper chamber was removed, and the cells were immobilized in 4% paraformaldehyde for 30 min, and then stained with 0.1% methylrosanilinium chloride. At least 10 photos of each group were taken by the upright microscope (Leica Microsystems, Ontario, Canada).

### 2.6.3. Osteogenic differentiation assay

The osteogenic differentiation properties of the Mg alloys were evaluated by culturing rat bone marrow mesenchymal stem cells (rBMSCs,  $2 \times 10^4$  cells/ $\text{cm}^2$ ) in osteogenic induction medium containing 10% concentration extracts of Mg alloys. After 14 d of incubation, rBMSCs were treated by the staining of alkaline phosphatase (ALP, Beyotime, China).

### 2.6.4. Osteogenesis-related gene expression

qRT-PCR was performed using ChamQ SYBR qPCR Master Mix (Vazyme) on an ABI-7300 Real-Time PCR System (Applied Biosystems) to analyze the expression of osteogenesis-related genes, such as ALP, Col-1, OCN, and OSX, after 14 days of incubation. Total RNA was isolated from rBMSCs using FastPure® Cell/Tissue Total RNA Isolation Kit (Vazyme) and converted to cDNA with HiScript® III RT SuperMix (Vazyme). All the reactions were performed in triplicate with GAPDH as an internal control. The primers were listed in Table 1:

## 2.7. In vitro antibacterial activity

### 2.7.1. Antibacterial performance

Gram-negative *Porphyromonas gingivalis* (P. gingivalis, ATCC 33277) and Gram-positive *Staphylococcus aureus* (S. aureus, ATCC 25923) were utilized to evaluate the antibacterial activity of Mg, Mg-5Ag and Mg-9Ag. P. gingivalis was cultured in brain heart infusion (BHI) and BHI agar with hemin, vitamin K and defibrinated sheep blood as supplements. S. aureus was cultured in Luria-Bertani (LB) broth and LB agar. The sterile Mg alloys were immersed in BHI and LB broth at  $37^\circ\text{C}$  for 72 h to prepare extracts, and the extraction ratio was consistent with the in vitro cell evaluation. The bacterial suspension ( $10^6$  CFU/mL) was incubated with 10% concentration extracts of Mg alloys in 12-well plates. To analyze the bacterial growth rate, the OD values were read at 600 nm using a microplate reader at 0 h, 12 h, 24 h and 48 h. After 24h of incubation, the two species of bacterial suspension were diluted, respectively. The diluted solution (100  $\mu\text{L}$ ) was evenly spread on BHI agar plates and LB agar plates to count the forming colony units.

Table 1  
Primer Sequences for qRT-PCR.

Target gene	Forward primer sequence (5'–3')	Reverse primer sequence (3'–5')
GAPDH	ACCACAGTCCATGCCATCAC	TCCACCACCCTGTTGCTGTA
OSX	AAGAAGCCCATTCACAGC	CTTGCCACAGAAAAGCCA
OCN	ATCTTTCTGCTCACTCTGCT	CTACCTTATGCCCCTCCTG
ALP	CCTGACTGACCCTTCCCT	AATCCTGCCTCCTCCAC
Col-I	CCAGACGCAGAAGTCATA	CAAAGTTTCTCCAAGAC

### 2.7.2. Live/dead staining test

After 24 h of incubation, the two species of bacteria were washed twice using 0.85% NaCl solution and stained LIVE/DEAD® BacLight™ Bacterial Viability Kit (L7012, Invitrogen, USA). A confocal laser scanning microscopy was used to observe the bacteria viability.

### 2.7.3. TEM observation

Transmission electron microscopy (TEM, Hitachi-7600 machine, Tokyo, Japan) was performed to examine the intracellular changes in the two species of bacteria. After 24h of incubation, the bacteria were fixed with a mixture (1:1) of 2.5% (v/v) glutaraldehyde and 4% w/v paraformaldehyde at 4°C for 12h, and then were fixed in 1% (w/v) osmium tetroxide (O<sub>3</sub>O<sub>4</sub>) for 2h. After that, the bacteria were dehydrated in a series concentration of ethanol, and embedded in paraffin wax. The thin sections were cut by using an ultramicrotome (PowerTome-PC; RMC, America).

### 2.8. Statistical analysis

Data from a minimum of three independent experiments were analyzed using GraphPad 6.0 software and expressed as mean ± SD. Differences among three groups or more were analyzed by one-way ANOVA. P-values < 0.05 were considered as statistically significant.

## 3. Results

### 3.1. Microstructural evolution

Fig. 1 shows the microstructures evolution and the XRD diffraction patterns of Mg and Mg-Ag alloys, which were taken along the extrusion direction. Mg was mainly composed of coarse grains, and by alloying with the element Ag, the grain size of the Mg-Ag alloys gradually became finer. For Mg and Mg-5Ag, all diffraction peaks were identified as  $\alpha$ -Mg phase, while some other diffraction peaks with weak intensities were detected in Mg-9Ag, identified as Mg<sub>4</sub>Ag (Fig. 1d). It can be inferred that Ag element of Mg-5Ag approximately dissolve into the Mg matrix with a small amount of precipitation, which was also proved from Fig. 1b. In contrast, numerous secondary phase particles with bright contrast appeared in Mg-9Ag. Combined with the EDS and XRD analysis, the secondary phases were Mg<sub>4</sub>Ag compounds.

The EBSD analysis of Mg, Mg-Ag alloys is shown in Fig. 2. Mg and Mg-Ag alloys demonstrated basal texture

that plane of Mg matrix was parallel to the extrusion direction. In addition, the basal texture of Mg-Ag alloys became weaker with the increase of Ag content, and Mg-9Ag had the lowest texture intensity of 5.79. It can be observed that lots of low angle grain boundaries (LAGBs) in the unDRXed coarse grains of Mg (Fig. 2a), while there were fewer number of LAGBs in Mg-5Ag and Mg-9Ag. Mg-Ag alloys exhibited relatively homogeneous equiaxed grain structure, and the DRXed grains of Mg-Ag alloys had a more random texture, in which Mg-9Ag obtained a nearly fully DXRed grain structure. As shown in Fig. 2c, d and e, the grain size of Mg alloys was decreased with the increasing content of Ag. As a result, the average grain size of Mg was 41.4  $\mu$ m, while those of Mg-5Ag and Mg-9Ag were 28.5  $\mu$ m and 5.6  $\mu$ m, respectively.

### 3.2. Mechanical and degradation behavior

The mechanical behavior of Mg and Mg-Ag alloys was evaluated by static tensile and three-point bending tests, and the mechanical properties are shown in Fig. 3. The addition of Ag element significantly enhanced the yield strength (YS) and ultimate tensile strength (UTS) of Mg alloys, and the YS and UTS of Mg-9Ag can reach 205.7 MPa and 313.8 MPa, respectively. Mg-5Ag has a UTS of 259.3 MPa and the elongation at fracture of 26.1%. The presence of Ag also improved the bending resistance of Mg alloys. Mg, Mg-5Ag and Mg-9Ag can withstand a maximum load of 194.0 N, 373.6 N and 437.2 N, respectively. Compared with Mg, Mg-Ag alloys exhibited better bending ability at ambient temperature. When the maximum displacement was 5.5 mm, Mg-Ag alloys were bent, and no cracks were observed.

Fig. 4 displays the in vitro degradation behavior of Mg and Mg-Ag alloys. The surface morphologies of samples immersed in DMEM for 72h (Fig. 4a), and corrosion layers formed on samples with numerous microcracks and white contrast deposits. In addition, more microcracks and deposits can be observed on the corrosion layer of Mg-9Ag. The corrosion products were analyzed by ATR-FTIR, and it indicated that CO<sub>3</sub><sup>2-</sup>, PO<sub>4</sub><sup>3-</sup> and HPO<sub>4</sub><sup>2-</sup> bands appeared at 1300–1550 cm<sup>-1</sup>, 1000–1140 cm<sup>-1</sup> and 913–934 cm<sup>-1</sup>, respectively (Fig. 4d) [28]. The pH values and the concentration of released Ag<sup>+</sup> of Mg and Mg-Ag alloys in DMEM were measured (Fig. 4e, f). For the three groups, the pH values increased rapidly within 24h, then the growth trend gradually slowed down, and finally stabilized. The pH values of Mg-5Ag and Mg showed similar trends and were still lower

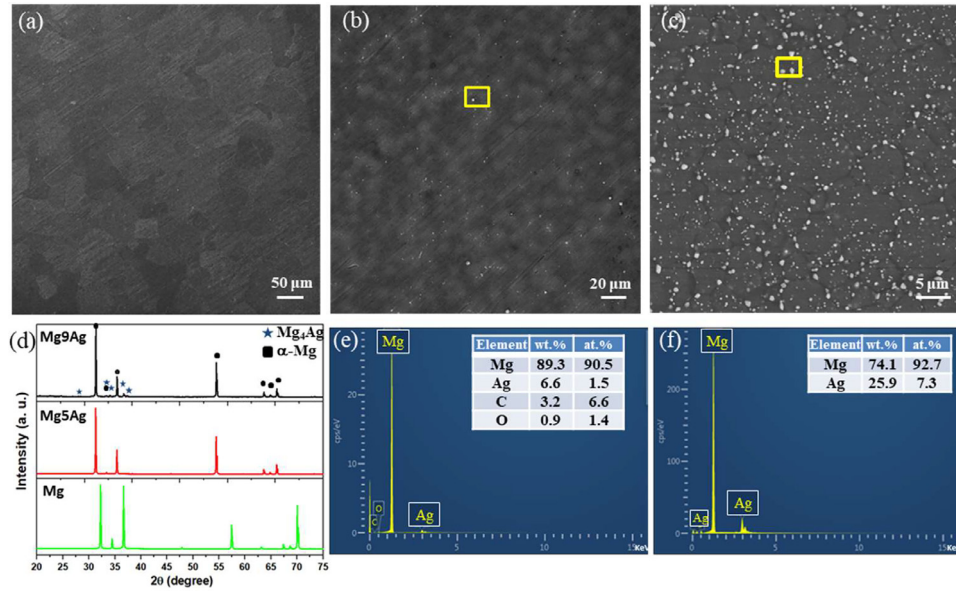


Fig. 1. Microstructure of (a) Mg, (b) Mg-5Ag, (c) Mg-9Ag, XRD patterns of Mg and Mg-Ag alloys, and quantified EDS spectra for the marked area of (e) Mg-5Ag and (f) Mg-9Ag alloys.

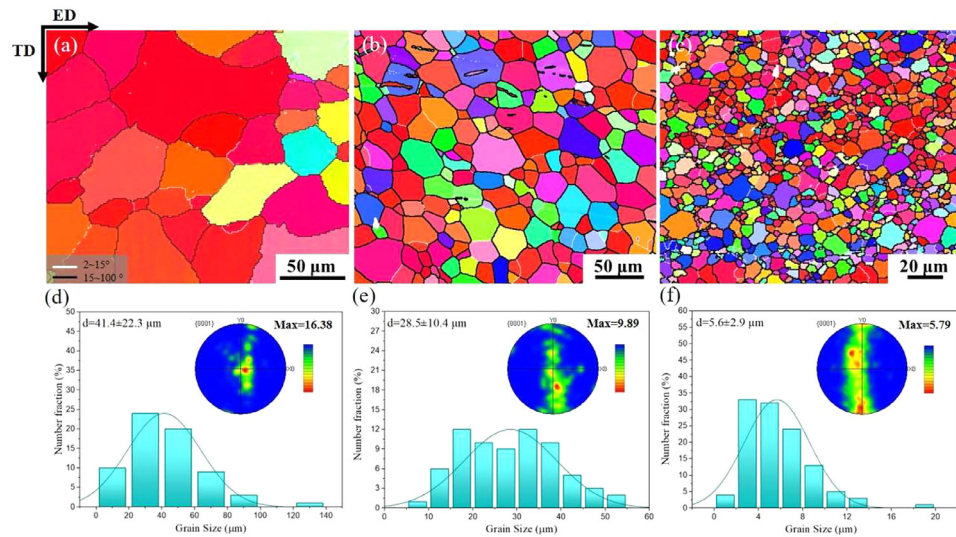


Fig. 2. Microstructure of (a) Mg, (b) Mg-5Ag, (c) Mg-9Ag, XRD patterns of Mg and Mg-Ag alloys, and quantified EDS spectra for the marked area of (e) Mg-5Ag and (f) Mg-9Ag alloys.

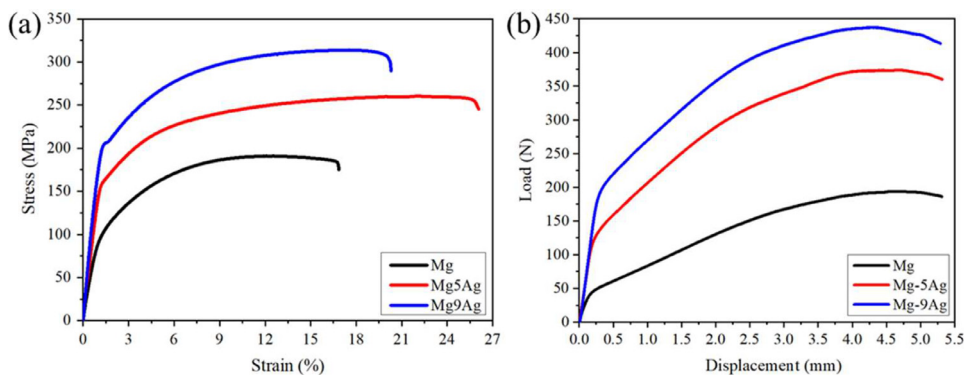


Fig. 3. (a) Tensile strain-stress curves and (b) bending displacement-load curves of Mg and Mg-Ag alloys.

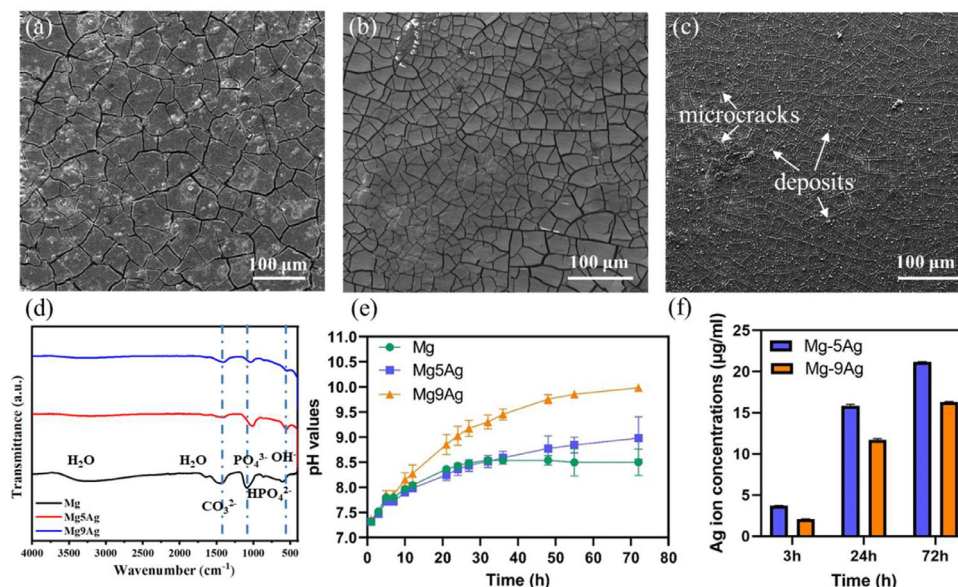


Fig. 4. Surface morphology of samples immersed in DMEM for 72h: (a) Mg, (b) Mg-5Ag, (c) Mg-9Ag, (d) ATR-FTIR spectra of the corrosion products, (e) the pH values evolution and (f) the concentration of cumulatively released  $\text{Ag}^+$  with a function of immersion time.

than 9 after soaking for 72h. Furthermore, the pH value of Mg-9Ag reached a maximum of 9.9 after soaking for 72h. The  $\text{Ag}^+$  concentration of Mg-5Ag was the highest, reaching  $21 \mu\text{g/mL}$  after soaking for 72h. The maximum  $\text{Ag}^+$  concentration released by Mg-Ag alloy is much lower than the cytotoxic content of mammalian cells ( $1200 \mu\text{g/mL}$ ) [29].

To further reveal the chemical composition of the corrosion products, the corroded samples were characterized by X-ray photoelectron spectroscopy (XPS) after soaking in DMEM (Fig. 5) [30]. XPS survey spectra display that Mg, O, Ca, P, C and limited Na elements were detected in three samples. The composition of corrosion products of Mg-5Ag was similar to that of Mg, and Ag element was not detected by XPS (Fig. 5a, b). The high-resolution Mg 2p spectra of Mg-5Ag are shown in Fig. 5d, Mg 2p peak was distributed from 47.0 to 52.8 eV, which can be fitted by  $\text{Mg}^0$  at 49.5 eV,  $\text{Mg}^{2+}$  at 50.6 eV. Noted that, O bonding states can be associated with metal hydroxide/carbonate ( $\sim 532$  eV), metal oxides (530.5 eV). The C 1s spectra reveal more about the surface bonding states, which show a sharp main peak of 284.8 eV originating from C-C, and the broad peak at 288.5 eV should be attributed to metal carbonate. Specifically, the P 2p spectra are likely associated with a typical phosphonic group peak at 133.5 eV. Besides, Ca 2p peak assigned to 347.0 eV, accompanied by C 1s at 288.5 eV and O 1s at 530.5 eV was detected. Combined with the ATR-FTIR results, it indicates the possible presence of Mg-O, Mg-OH, Mg- $\text{CO}_3$ , Mg- $\text{PO}_4$ , Ca- $\text{PO}_4$  and Ca- $\text{CO}_3$  binding. Notably, Ag and Cl elements were detected in the corrosion products of Mg-9Ag. The high-resolution Ag 3d spectra consist of two individual peaks at 373.4 eV and 367.4 eV, accompanied by Cl 2p at 199.27 and 197.67 eV, ascribed to the Ag-dominated corrosion products of AgCl (Fig. S1, supporting information).

The degradation behavior of Mg alloys was evaluated by potentiodynamic polarization (PDP) and electrochemical impedance spectroscopy (EIS) in DMEM, as depicted in Fig. 6. Mg alloys with higher Ag content exhibited higher open-circuit potential (OCP) after immersion for 900 s, and the OCP of Mg, Mg-5Ag and Mg-9Ag was  $-1.95 \pm 0.02 V_{\text{SHE}}$ ,  $-1.74 \pm 0.02 V_{\text{SHE}}$  and  $-1.67 \pm 0.03 V_{\text{SHE}}$ , respectively. Alloying element Ag showed little effect on the anode dissolution rate, while accelerating the cathodic process of Mg alloys, which is consistent with the phenomenon observed in Mg-Mn-Ag alloys by Yang et al. [31]. The anodic polarization curves of Mg-Ag alloys present pseudo-passivation characteristics, and the pitting potentials of Mg-Ag alloys are around  $-1.37 V_{\text{SHE}}$ , which implies partially pseudo-protective films on the surface of Mg-Ag alloys. The corresponding electrochemical parameters derived from the polarization curves: corrosion potential ( $E_{\text{corr}}$ ), corrosion current density ( $I_{\text{corr}}$ ), cathodic slope ( $\beta_c$ ), corrosion resistance ( $R_p$ ) and corrosion rate ( $V_{\text{PDP}}$ ) are listed in Table 2. Although the addition of Ag moved  $E_{\text{corr}}$  of Mg alloys to a more positive direction, it also enhanced  $I_{\text{corr}}$ , resulting in a decrease of  $R_p$ . The Nyquist curves of Mg alloys all exhibited two capacitive loops: the high-frequency capacitive loop represented the film resistance, and the medium-frequency capacitive loop related to the relaxation of the mass transport in the solid phase was a result of the formation of the corrosion product film. Therefore, the decreasing order of corrosion rate: Mg-9Ag > Mg-5Ag > Mg.

### 3.3. In vitro biological evaluation

#### 3.3.1. Cytotoxicity and cell migration

Fig. 7 shows the relative L929 cells viability incubated in different concentrations of Mg alloy extracts for 24h. The cytocompatibility of Mg alloy extracts on L929 cells can be im-

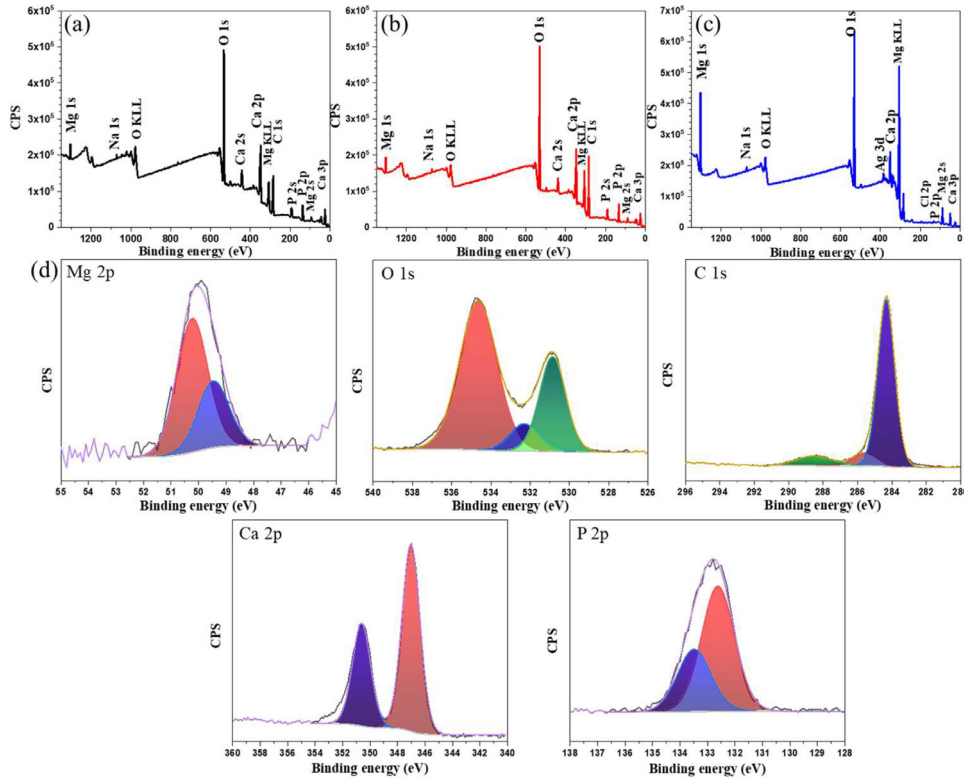


Fig. 5. XPS analysis of the corrosion products: (a) Mg, (b) Mg-5Ag, (c) Mg-9Ag and (d) typical high-resolution narrow scan results of Mg 2p, O 1s, Ca 2p, P 2p and C 1s for the corroded Mg-5Ag.

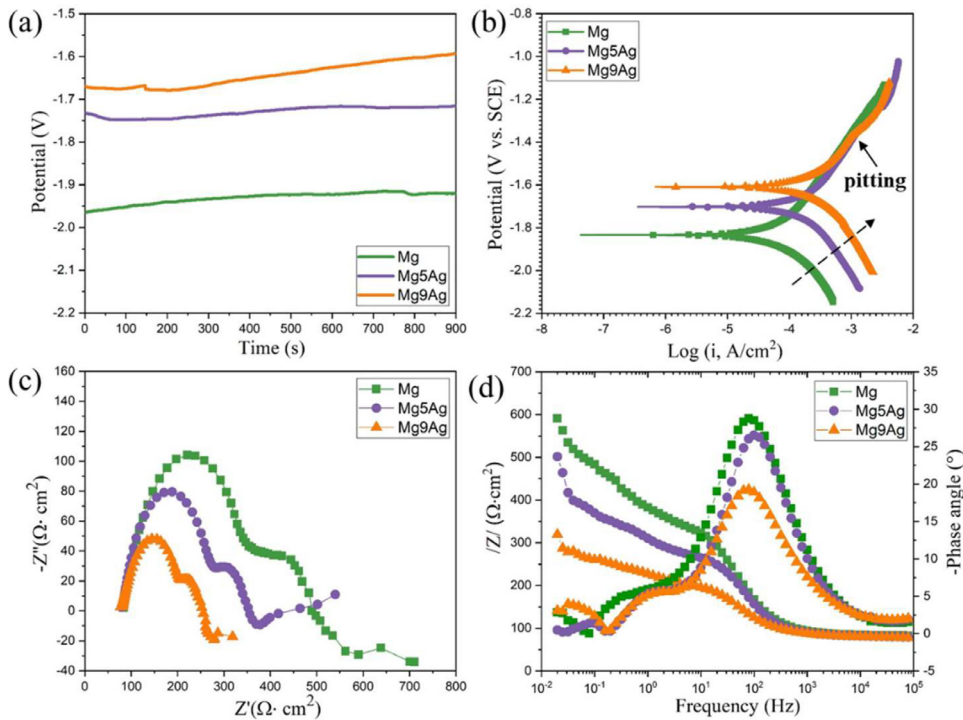


Fig. 6. Electrochemical behavior of Mg and Mg-Ag alloys immersed in DMEM: (a) Evolution of open-circuit potential, (b) Potentiodynamic polarization curves, (c) Nyquist diagram, (d) Bode and phase angle diagrams.

Table 2  
Electrochemical parameters of Mg based membranes derived from Fig. 6b, and corrosion rates measured by weight loss.

Samples	$E_{\text{corr}}$ (V)	$I_{\text{corr}}$ ( $\text{A}\cdot\text{cm}^{-2}$ )	$\beta_c$ ( $\text{mV}\cdot\text{dec}^{-1}$ )	$R_p$ ( $\Omega\cdot\text{cm}^{-2}$ )	$V_{\text{PDP}}$ ( $\text{mm}\cdot\text{y}^{-1}$ )	$V_{\Delta W}$ ( $\text{mm}\cdot\text{y}^{-1}$ )
Mg	-1.84	$4.77 \times 10^{-5}$	231.1	1138.1	1.04	1.47
Mg-5Ag	-1.70	$1.60 \times 10^{-4}$	292.0	403.4	3.49	2.49
Mg-9Ag	-1.61	$2.23 \times 10^{-4}$	251.4	248.2	4.86	4.88

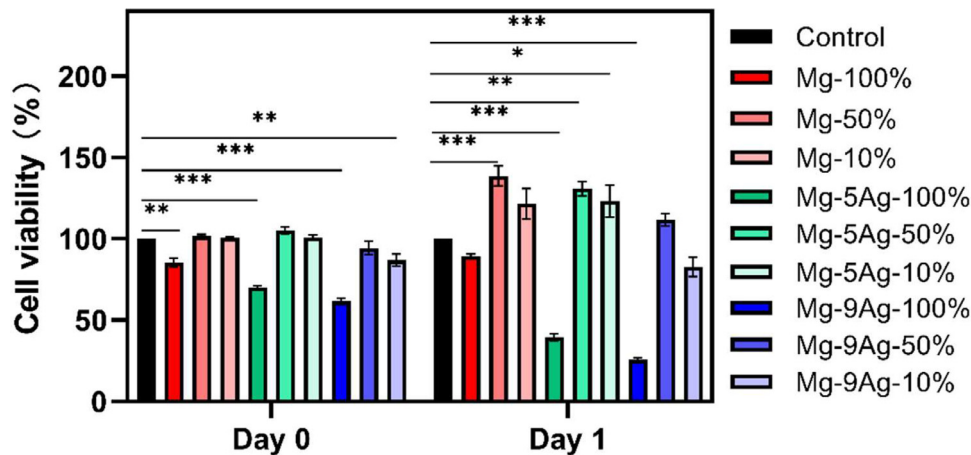


Fig. 7. Cytotoxicity of L929 cells incubated with different concentrations of Mg alloy extracts (Data presented as mean  $\pm$  SEM, \* $P$  < 0.05, \*\* $P$  < 0.01, \*\*\* $P$  < 0.001).

proved by dilution. Compared with the control group, all 50% concentrations of Mg alloy extracts can significantly promote L929 cell viability, among which Mg-5Ag and Mg showed similar trends. Notably, further dilution of Mg alloy extracts to concentrations of 10% decreased cell viability in all groups.

To clarify how Mg-Ag alloys affect the cell migration behavior, both scratch and transwell migration assays were conducted (Fig. 8). Compared with the control group, faster wound closure of L929 cells incubated in the Mg and Mg-Ag groups was observed. In particular, the Mg-Ag groups positively affected the migration behavior of L929 cells. The Mg-9Ag group exhibited the smallest scratch area, and the wound closure rate reached around 50% after 24h. In addition, L929 cells tended to move to the lower chamber containing Mg and Mg-Ag alloy extracts. More L929 cells were observed in the Mg groups with higher Ag contents, and exhibited fiber fusiform shape. These results suggested that Mg-Ag alloys had a significantly promotive effect on the migration behavior of L929 cells, which was beneficial to wound healing.

### 3.3.2. Osteogenic differentiation performance

We explore the effect of Mg alloys on the osteogenic differentiation behavior of BMSCs. ALP activity is an early osteogenic marker, and evaluated by ALP staining on BMSCs cultured in Mg alloy extracts for 14d (Fig. 9a). The ALP results showed that there was no significant difference between the Mg group, the Mg-Ag groups and the control group cultured in osteogenic induction medium. For Alizarin Red S staining, mineralization nodules deposition of all the groups also revealed no significant difference (Fig. 9b). To further investigate the osteogenic effect at the gene level, the osteogenesis-related genes: Col-I, ALP, OCN and OSX by

qRT-PCR (Fig. 9c). The expression level of the osteogenesis-related genes was increased in Mg and Mg-Ag groups, and significantly upregulated in Mg-9Ag group. Specifically, OCN levels are indicative of the bone formation rate, while OSX is associated with osteoblast differentiation and bone mineralization. The Mg-9Ag group exhibited notably favorable responses in both OCN and OSX detection, suggesting an enhanced support for osteogenic differentiation.

### 3.3.3. Antibacterial activity

To evaluate the antibacterial effect of Mg-Ag alloys, Gram-negative *Porphyromonas gingivalis* (*P. gingivalis*) and Gram-positive *Staphylococcus aureus* (*S. aureus*) were cultured in Mg alloy extracts, respectively. First, the growth curves of two kinds of bacteria within 48h are depicted in Fig. 10a and c. Compared with the control group, the OD values of both bacteria in the Mg and Mg-Ag groups exhibited minimal increases as the incubation time progressed. Notably, the OD value in the Mg-Ag group remained consistently low at 48h, but the Mg group displayed a rising trend. Second, the plating gradient dilution method was also employed to confirm the number of bacterial colonies at 24h (Fig. 10e and f). Consistently, the Mg-Ag group exhibited a significant decrease in the number of bacterial colonies on plates compared with the control and Mg groups, suggesting that both Mg-5Ag and Mg-9Ag groups have effective antibacterial activity. The summarized colony counts are presented in Fig. 10b and d. Remarkably, the Mg-9Ag group demonstrated almost no formation of bacterial colonies, highlighting its superior antibacterial performance against *P. gingivalis* and *S. aureus*.

The morphology of bacteria cultured in Mg alloy extracts was further observed by TEM (Fig. 11). Both *S. aureus* and *P.*

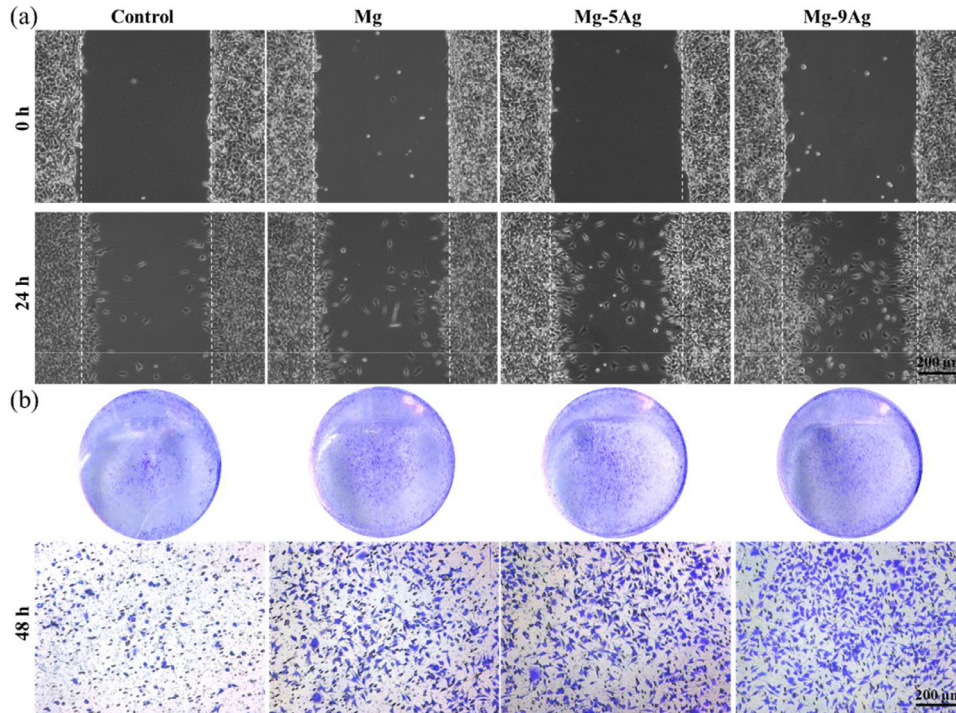


Fig. 8. The migration behavior of L929 cells cultured in Mg alloy extracts: (a) scratch assay and (b) transwell migration assay.

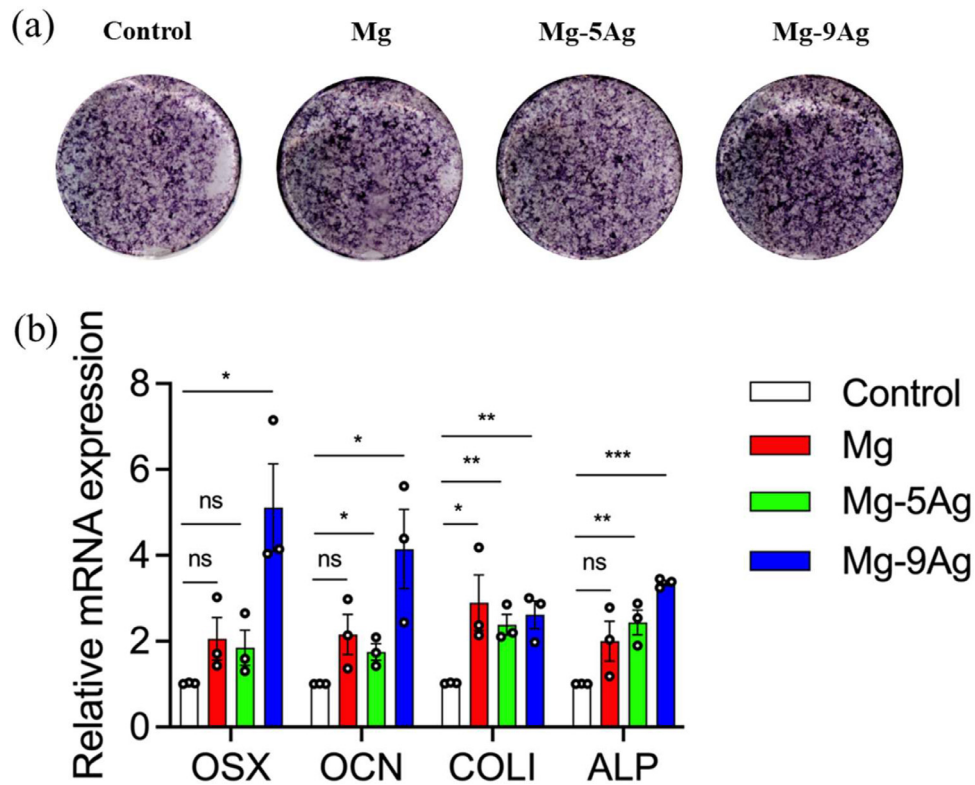


Fig. 9. Osteogenic differentiation behavior of rBMSCs cultured in Mg alloy extracts: (a) ALP staining, (b) Alizarin Red S staining, and (c) relative expression of osteogenic differentiation marker genes in rBMSCs cultured for 14 days (Data presented as mean  $\pm$  SEM, \* $P$  < 0.05, \*\* $P$  < 0.01, \*\*\* $P$  < 0.001).

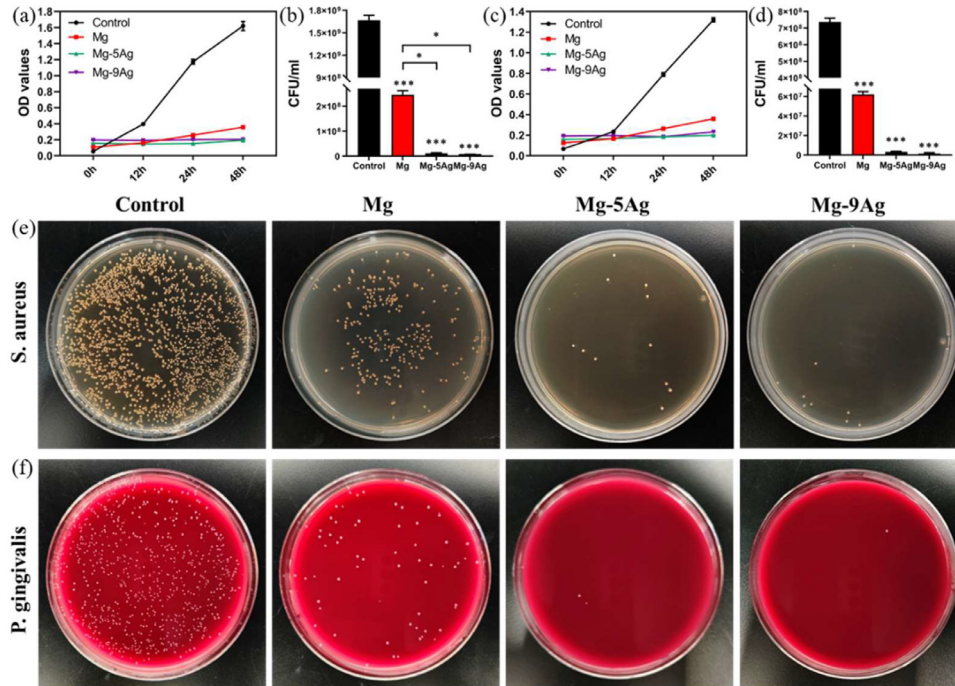


Fig. 10. In vitro antibacterial performances of Mg alloys: (a) growth curves of *S. aureus* cultured in Mg alloy extracts within 48h, (b) colony counts of *S. aureus* after 24 h, (c) the growth curves of *P. gingivalis* cultured in Mg alloy extracts within 48h, (d) colony counts of *P. gingivalis* after 24 h. Representative images of (e) *S. aureus* and (f) *P. gingivalis* grown in Mg alloy extracts after 24 h. (Data presented as mean  $\pm$  SD, \* $p$  < 0.05, \*\* $p$  < 0.01, \*\*\* $P$  < 0.001).

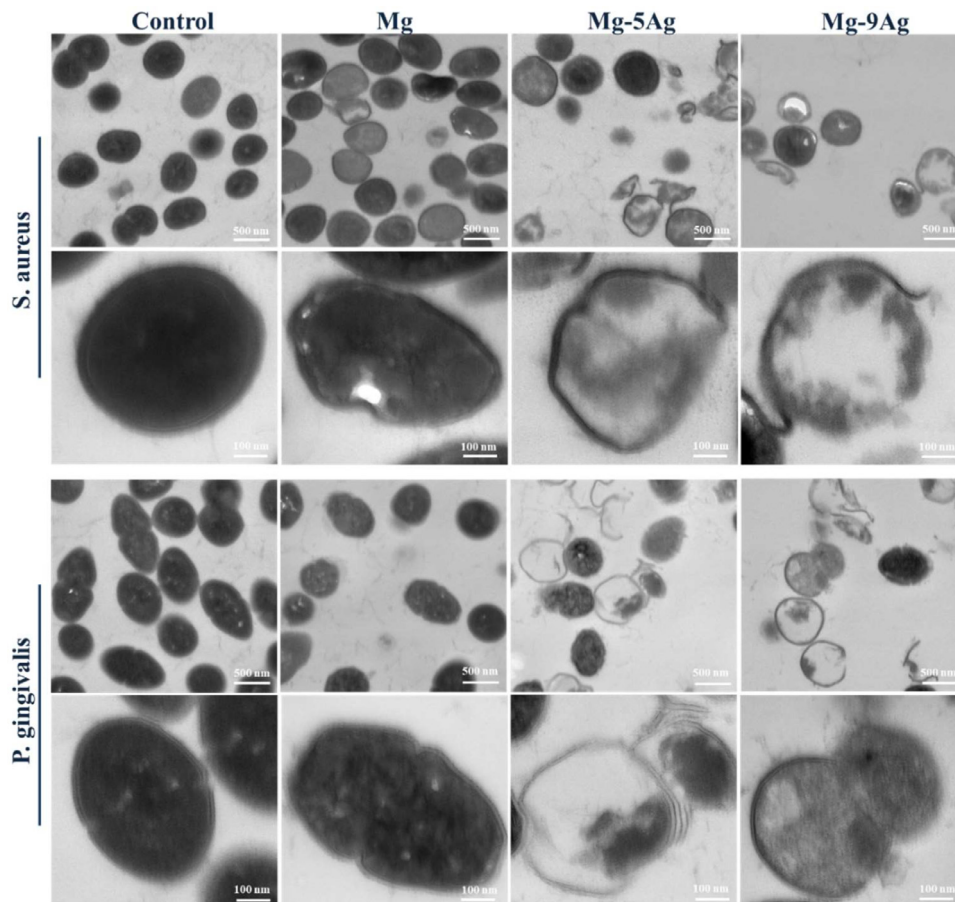


Fig. 11. Bacteria morphologies of *S. aureus* and *P. gingivalis* cultured in Mg alloy extracts visualized by TEM after 24h.

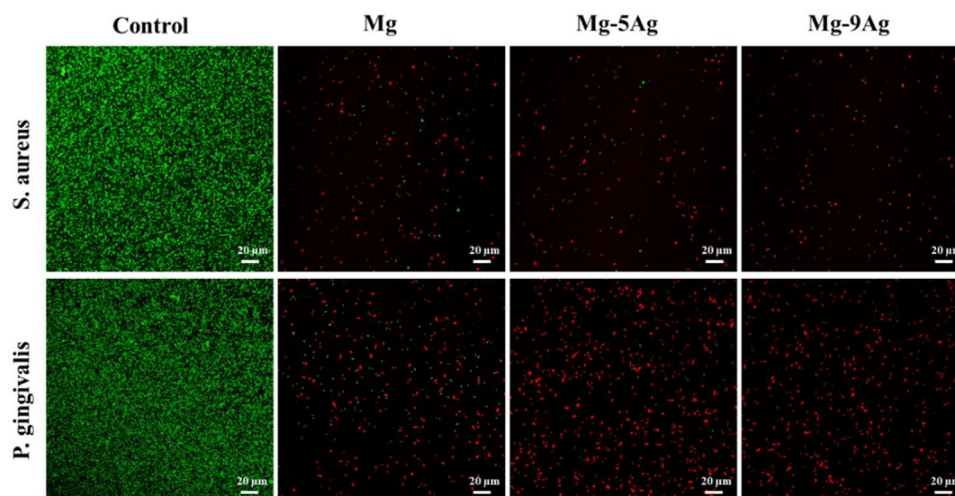


Fig. 12. Confocal laser scanning microscopy images of live/dead bacteria staining after 24 h (Live bacteria stained green, and dead bacteria stained red).

gingivalis show a healthy morphology and normal binary fission in the control group. In the pure Mg group, the cell walls of the majority of bacteria experienced shrinkage, while some bacteria could still perform normal binary fission. However, the morphologies of *S. aureus* and *P. gingivalis* were abnormal in the Mg-5Ag and Mg-9Ag groups. Notably, compared with the pure Mg group, the separation of cell membrane from cell wall and the outflow of cytoplasm were observed in the Mg-5Ag and Mg-9Ag groups. Fig. 12 depicts the bacteriostatic activity of *S. aureus* and *P. gingivalis* cultured in Mg alloy extracts, as detected using confocal laser scanning microscopy (CLSM). The control group shows a high intensity of green fluorescence, indicating the formation of a bacterial biofilm. In the pure Mg group, the green fluorescence intensity was significantly reduced. In contrast, only a small number of weak green fluorescent spots were observed in the Mg-5Ag group, and almost no live bacteria were detected in the Mg-9Ag group. Therefore, these results confirmed that Mg-5Ag and Mg-9Ag can act as not only a structural barrier but also a defense against bacterial invasion.

#### 4. Discussions

The GTR/GBR membrane is a crucial intervention strategy for reconstructing of periodontal tissues [32]. In fact, the ideal GTR/GBR membranes should not only possess sufficient mechanical properties as physical barrier membranes but also exhibit exceptional antibacterial performance to effectively prevent postoperative infections [33]. Recent researches put forward that Mg-Ag alloys had good antibacterial effects [34,35]. However, there is a lack of comprehensive understanding regarding the mechanism by which Mg-Ag alloys act against bacteria, particularly their feasibility in combating periodontal pathogens. Furthermore, simultaneously balancing the mechanical property and corrosion resistance of Mg alloys remains a significant challenge, as these two properties are often mutually exclusive.

Ag plays a solid solution strengthening role, and also is an important age hardening element in Mg alloys [36]. Xiao et al. [37] reported nanocrystalline Mg-Ag alloys obtained by conventional cold rolling, which is attributed to the segregation of abundant Ag along the nanograin boundaries. Referring to the binary phase diagram of Mg-Ag, the solubility of Ag in Mg diminishes as the temperature decreases, leading to Ag precipitates at the interface. These studies align with our observation in Fig. 1, where Ag elements were predominantly situated along the grain boundaries of Mg-5Ag alloy, thereby altering the stacking fault energy and *c/a* ratio, subsequently influencing the dynamic recrystallization (DRX) during the hot extrusion process. When the Ag content was further increased to 9 wt.%, exceeding the maximum solubility of Ag in the Mg matrix, a great number of Mg<sub>4</sub>Ag second phases precipitated at the grain boundaries. The oversaturated Ag plays a crucial role in pinning crystal defects and hindering dynamic recovery [38]. In addition, the formation of Mg<sub>4</sub>Ag second phases further impede the growth of DRXed grains through the particle-stimulated nucleation (PSN) effect [39]. In a word, as the Ag content increases, the precipitation of numerous second phases leads to the formation of larger and wider recrystallization nuclei. It effectively refines the grains and contributes to the attenuation of the overall texture with random orientation. Consequently, the mechanical properties of Mg-Ag alloys exhibit significant improvements compared with pure Mg. The tensile stress of commercially available bioabsorbable Bio-Gide® membrane is reported to be 3.7 MPa [40]. However, the mechanical properties of Mg-Ag alloys surpass those of commercially available bioabsorbable barrier membranes. The mechanical properties indicate that Mg-Ag alloys exhibit enhanced resistance to external pressure exerted by soft tissues during implantation, ensuring minimal risk of collapse and higher safety levels.

However, the addition of Ag is conventionally deemed detrimental to the corrosion resistance of Mg alloys against the inorganic solutions, especially when an excess of the second phases is formed in Mg matrix [41]. It is reported that

increasing the Ag content of as-cast Mg-Ag alloys, the secondary dendrites remarkably increased inside the grains, and the continuous  $\beta$ -Mg<sub>4</sub>Ag phases were reticulated in Mg matrix [34]. These  $\beta$ -Mg<sub>4</sub>Ag phases are considered effective cathodic sites for the hydrogen evolution reaction, leading to accelerated micro-galvanic corrosion. To limit the impact of micro-galvanic corrosion, previous studies have focused on enhancing the corrosion resistance of as-cast Mg-Ag alloys by employing heat treatment to minimize the presence of secondary dendrites [42]. Although this approach has proven effective in enhancing the corrosion resistance of Mg-Ag alloys, the incremental addition of Ag had a negligible impact on the corrosion rate after heat treatment, significantly reducing antibacterial performance. In this study, we utilized extrusion to eliminate the dendritic microstructure in the as-cast Mg-Ag alloy. This process prevented the continuous distribution of  $\beta$ -Mg<sub>4</sub>Ag phases, ultimately yielding a uniform microstructure with refined grains. When Mg-5Ag and Mg-9Ag were immersed in DMEM, the main corrosion products, Mg(OH)<sub>2</sub> and MgO, were detected in Fig. 5. Simultaneously, Fig. S2 indicates that the Ca/P atomic ratio of the corrosion products on Mg-5Ag is less than 1. In the presence of phosphate, calcium and magnesium within the solution, a precipitation sequence occurred due to the differences in the solubility product constant ( $K_{sp}$ ). Calcium phosphate precipitated first, followed by the formation of magnesium phosphate [43]. Additionally, the abundance of carbonate buffer in DMEM facilitated the formation of magnesium carbonate. Ultimately, the development of a denser protective film consisting of calcium phosphate, magnesium phosphate, and magnesium carbonate aids in impeding pitting corrosion, thereby enhancing corrosion resistance of Mg-Ag alloys in the long term. In addition, the corrosion product AgCl was detected on the surface of Mg-9Ag (Fig. S1). Consequently, the detected Ag<sup>+</sup> ion concentration in Mg-9Ag soaked in DMEM is lower than that in Mg-5Ag. Despite the slightly increased corrosion rate, the risk of pitting corrosion diminishes, and all the Mg-Ag alloys exhibited acceptable general corrosion compared to pure Mg.

Two predominant perspectives emerge in the realm of antibacterial strategies for Ag-containing alloys: the released metal ions antibacterial strategy and the contact-killing antibacterial strategy [44,45]. In contrast to the reported antibacterial effect of Ti-Ag alloys primarily controlled by the precipitation of Ti<sub>2</sub>Ag for contact sterilization [46], the precipitation of second phases in Mg-Ag alloys minimally affects bacterial adhesion. Tie et al. [34] found that all T4 treated as-cast Mg-Ag alloys exhibited improved antibacterial activity compared with pure Mg, when co-cultured with two Staphylococcus strains. The improved antibacterial effects, particularly evident with higher Ag content (~6 wt.%), notably reduced the number of adherent bacteria (by up to 75%) and suppressed bacterial activity (by up to 79%). Given that the  $\beta$ -Mg<sub>4</sub>Ag phases of T4 treated Mg-Ag alloys were nearly dissolved into the Mg matrix, we hypothesize that the antibacterial efficacy of the Mg-Ag alloy primarily stems from the release of Ag<sup>+</sup> facilitated by the corrosion of the alloy. In this study, Mg alloy extracts were adapted to culture with *P. gingivalis* and

*S. aureus* to eliminate the influence of contact sterilization. Combining TEM and CLSM images (Figs. 11 and 12), it can be observed that the bacterial membrane of the Mg group shrank due to the alkalinity induced by OH<sup>-</sup> ions generated during corrosion. In contrast, the Mg-Ag groups demonstrate superior antibacterial effects, evident in cytoplasmic leakage and bacterial death. It suggests that the antibacterial effect is influenced by the corrosion products of Mg-Ag groups, particularly the released Ag<sup>+</sup> ions and AgCl precipitates. When the Mg-Ag alloy was immersed in DMEM, an electrode potential difference between the Mg<sub>4</sub>Ag second phases and the Mg matrix triggered rapid corrosion of the adjacent Mg matrix. This corrosion resulted in the detachment of the second phases from the matrix, which were corroded to generate Ag<sup>+</sup> and Mg<sup>2+</sup> ions. In addition, due to the significantly lower  $K_{sp}$  of AgCl compared to AgOH [47], the Ag<sup>+</sup> ions generated by corrosion initially reacted with Cl<sup>-</sup> ions in DMEM, resulting in the formation of AgCl, which precipitates on the surface of Mg-Ag alloys.

The AgCl precipitates directly act on the cell wall, membrane proteins, and glycoproteins of bacteria, thereby disrupting normal metabolism and substance exchange [48]. Additionally, Ag<sup>+</sup> ions penetrate the bacteria through ion channels on the cell membrane, impacting physiological functions [49]. The kinetics of released Ag<sup>+</sup> ions and AgCl precipitates are closely associated with the corrosion process. With increasing Ag content, cathodic activation of the Mg-Ag alloy significantly intensifies. This activation results from dissolving Mg<sub>4</sub>Ag second phases and subsequently forming AgCl particles through redeposition, creating more efficient cathodes with increased surface area. AgCl redeposition, serving as an effective cathode site for the hydrogen evolution reaction, plays a crucial role in this autocatalytic process. Therefore, the Mg-Ag alloys ensure a sustained release of Ag, establishing a long-lasting antibacterial effect.

Furthermore, Mg-Ag alloys demonstrate acceptable cytocompatibility, promoting both cell migration and osteogenesis. This phenomenon appears to be linked to the concentration of corrosion products from the Mg-Ag alloys. Abundant reports have extensively explored the mechanisms through which Mg<sup>2+</sup> ions, in conjunction with an alkaline environment, facilitate osteogenic differentiation [50–52]. It demonstrates that a moderate quantity of Mg<sup>2+</sup> ions can promote the expression of osteogenesis-related genes via the canonical Wnt signaling pathway [53]. Additionally, when the content of Ag<sup>+</sup> ions is at low levels, it exhibits no adverse effects on the adhesion, proliferation, and differentiation of osteoblasts [29,54]. The results depicted in Fig. 9b reveal that pure Mg elicits an impact on the osteogenic differentiation; however, its efficacy appears constrained, likely attributed to the concentration of released Mg<sup>2+</sup> ions. Conversely, alloying with Ag element not only facilitates the corrosion of Mg alloys to a certain extent but also regulates the release of Ag<sup>+</sup> and Mg<sup>2+</sup> ions by managing the Ag content. The synergistic release of Ag<sup>+</sup> and Mg<sup>2+</sup> ions of Mg-Ag alloys exhibits the osteogenic differentiation potential during the initial stage of osteogenesis. Furthermore, Zhao et al. [55] introduced co-doping of

Ag<sup>+</sup> and Mg<sup>2+</sup> ions into bioinert Ti, the coordinated release of Ag<sup>+</sup> and Mg<sup>2+</sup> ions has been shown to boost the expression of osteogenesis-related genes, such as Runx2, ALP, OCN, and Col-I. Yang et al. [56] fabricated Mg(OH)<sub>2</sub>/Ag<sub>2</sub>O nanocomposites aimed at stimulating bone formation by facilitating the expression of OPG genes, which impede osteoclast differentiation through the synchronized release of Mg<sup>2+</sup> and Ag<sup>+</sup> ions. As a result, biodegradable Mg-Ag alloys, endowed with long-lasting antibacterial performance, improved cell migration and osteogenic differentiation, exhibit great potential as effective GBR/GTR membranes for periodontal tissue regeneration.

## 5. Conclusion

In this study, the feasibility of the newly developed Mg-Ag alloys as potential GBR/GTR membranes was explored. The mechanical stability, degradation behavior and biological performance of Mg-Ag alloys were investigated, and the main conclusions can be drawn:

- (1) Compared with pure Mg, Mg-Ag alloys demonstrate superior tensile strength, flexural strength, and improved plasticity, which can be ascribed to the weaker basal texture and finer grain structure.
- (2) Alloying with Ag, which accelerated the cathodic reaction of Mg alloys, resulted in slightly elevated electrochemical corrosion rates of Mg alloys compared with pure Mg in DMEM. Nevertheless, Mg-Ag alloys exhibited an acceptable general corrosion.
- (3) In vitro, the Mg-Ag alloys upregulated the expression of osteogenesis-related genes (Col-I, ALP, OCN and OSX) in rBMSCs and facilitated the migration of L929 cells, demonstrating the potential to promote healing in periodontal tissue.
- (4) The antibacterial effects of Mg-Ag alloys against *P. gingivalis* and *S. aureus* were primarily controlled by their corrosion products, encompassing released Ag<sup>+</sup> ions and AgCl precipitates.

## Declaration of competing interest

The authors declare that they have no known competing financial interests or personal relationships that could have appeared to influence the work reported in this paper.

Xianhua Chen and Fusheng Pan are an editorial board member/editor-in-chief for Journal of Magnesium and Alloys and were not involved in the editorial review or the decision to publish this article. All authors declare that there are no competing interests.

## CRedit authorship contribution statement

**Sihui Ouyang:** Writing – original draft, Methodology, Investigation, Funding acquisition, Data curation, Conceptualization. **Xiong Wu:** Formal analysis, Data curation. **Li Meng:** Methodology, Data curation. **Xuerui Jing:** Data curation.

**Liying Qiao:** Validation, Methodology. **Jia She:** Writing – review & editing, Validation. **Kai Zheng:** Writing – review & editing, Investigation. **Xianhua Chen:** Validation, Supervision, Funding acquisition. **Fusheng Pan:** Supervision, Project administration, Funding acquisition.

## Acknowledgement

This study was supported by the National Natural Science Found for Distinguished Young Scholars (52225101), the National Natural Science Found (52301132), the China Postdoctoral Science Foundation (2022M720551), the Natural Science Foundation of Chongqing (CSTB2023NSCQ-MSX0527), the Chongqing Academician Special Fund (2022YSZX-JCX0014CSTB), and the Chongqing Science and Technology Commission (CSTB2022NSCQ-MSX0416).

## Supplementary materials

Supplementary material associated with this article can be found, in the online version, at doi:10.1016/j.jma.2024.03.022.

## References

- [1] R. Shi, J. Ye, W. Li, J. Zhang, J. Li, C. Wu, J. Xue, L. Zhang, *Mater. Sci. Eng. C. Mater. Biol. Appl.* 100 (2019) 523–534.
- [2] M.C. Bottino, V. Thomas, G. Schmidt, Y.K. Vohra, T.M. Chu, M.J. Kowolik, G.M. Janowski, *Dent. Mater.* 28 (2012) 703–721.
- [3] Y. He, X. Wang, Y. He, X. Zhao, J. Lin, Y. Feng, J. Chen, F. Luo, Z. Li, J. Li, H. Tan, *J. Mater. Chem. B* 10 (2022) 2602–2616.
- [4] X. Liu, X. He, D. Jin, S. Wu, H. Wang, M. Yin, A. Aldalbahi, M. El-Newehy, X. Mo, J. Wu, *Acta Biomater.* 108 (2020) 207–222.
- [5] M. Sun, Y. Liu, K. Jiao, W. Jia, K. Jiang, Z. Cheng, G. Liu, Y. Luo, *J. Mater. Chem. B* 10 (2022) 765–778.
- [6] J.M. Cordeiro, V.A.R. Barao, E.D. de Avila, J.F.A. Husch, F. Yang, J. van den Beucken, *Biomater. Adv.* 139 (2022) 212976.
- [7] J.M. Carbonell, I.S. Martin, A. Santos, A. Pujol, J.D. Sanz-Moliner, J. Nart, *Int. J. Oral Maxillofac. Surg.* 43 (2014) 75–84.
- [8] P. Aprile, D. Letourneur, T. Simon-Yarza, *Adv. Healthc. Mater.* 9 (2020) e2000707.
- [9] J. Wang, L. Wang, Z. Zhou, H. Lai, P. Xu, L. Liao, J. Wei, *Polymers* (2016) 8.
- [10] J. Wang, Y. Qu, C. Chen, J. Sun, H. Pan, C. Shao, R. Tang, X. Gu, *Mater. Sci. Eng. C. Mater. Biol. Appl.* 104 (2019) 109959.
- [11] Y. Liu, T. Li, M. Sun, Z. Cheng, W. Jia, K. Jiao, S. Wang, K. Jiang, Y. Yang, Z. Dai, L. Liu, G. Liu, Y. Luo, *Acta Biomater.* 146 (2022) 37–48.
- [12] I. Elgali, O. Omar, C. Dahlin, P. Thomsen, *Eur. J. Oral Sci.* 125 (2017) 315–337.
- [13] W. Zhang, P. Li, G. Shen, X. Mo, C. Zhou, D. Alexander, F. Rupp, J. Geis-Gerstorfer, H. Zhang, G. Wan, *Bioact. Mater.* 6 (2021) 975–989.
- [14] D. Porrelli, M. Mardirossian, L. Musciacchio, M. Pacor, F. Berton, M. Crosera, G. Turco, *ACS Appl. Mater. Interfaces* 13 (2021) 17255–17267.
- [15] Y. Ding, C. Wen, P. Hodgson, Y. Li, *J. Mater. Chem. B* 2 (2014) 1912–1933.
- [16] D.A. Robinson, R.W. Griffith, D. Shechtman, R.B. Evans, M.G. Conzemius, *Acta Biomater.* 6 (2010) 1869–1877.
- [17] W. Zhou, J. Yan, Y. Li, L. Wang, L. Jing, M. Li, S. Yu, Y. Cheng, *Y. Zheng, Biomater. Sci.* 9 (2021) 807–825.
- [18] J. Si, H. Shen, H. Miao, Y. Tian, H. Huang, J. Shi, G. Yuan, G. Shen, *J. Magnes. Alloy* 9 (2021) 281–291.

- [19] Z. Fan, B. Liu, J. Wang, S. Zhang, Q. Lin, P. Gong, L. Ma, S. Yang, *Adv. Funct. Mater.* 24 (2014) 3933–3943.
- [20] X. Zhang, Y. Zhang, Y. Lv, Z. Dong, L. Yang, E. Zhang, T. Hashimoto, X. Zhou, *J. Magnes. Alloy* 11 (2023) 2182–2195.
- [21] K. Bryla, J. Horky, M. Krystian, L. Litynska-Dobrzynska, B. Mingler, *Mater. Sci. Eng. C. Mater. Biol. Appl.* 109 (2020) 110543.
- [22] Z. Liu, R. Schade, B. Luthringer, N. Hort, H. Rothe, S. Muller, K. Liefeth, R. Willumeit-Romer, F. Feyerabend, *Oxid. Med. Cell Longev.* 2017 (2017) 8091265.
- [23] H. Chen, B. Yuan, R. Zhao, X. Yang, Z. Xiao, A. Aurora, B.A. Iulia, X. Zhu, A.V. Iulian, X. Zhang, *J. Magnes. Alloy* 10 (2022) 3380–3396.
- [24] J. Degner, F. Singer, L. Cordero, A.R. Boccaccini, S. Virtanen, *Appl. Surf. Sci.* 282 (2013) 264–270.
- [25] Z. Shi, M. Liu, A. Atrens, *Corros. Sci.* 52 (2) (2010) 579–588.
- [26] D.A. Jones, *Principles and prevention, Corrosion* 2 (1996) 168.
- [27] ISO 10993-12:2021 Biological evaluation of medical devices— Part 12: sample preparation and reference materials.
- [28] D. Bian, W. Zhou, J. Deng, Y. Liu, W. Li, X. Chu, P. Xiu, H. Cai, Y. Kou, B. Jiang, Y. Zheng, *Acta Biomater.* 64 (2017) 421–436.
- [29] M. Chen, E. Zhang, L. Zhang, *Mater. Sci. Eng. C. Mater. Biol. Appl.* 62 (2016) 350–360.
- [30] S. Ardizzzone, C. Bianchi, M. Fadoni, B. Vercelli, *Appl. Surf. Sci.* 119 (1997) 253–259.
- [31] L. Yang, Y. Shi, L. Shen, E. Zhang, G. Qin, X. Lu, X. Zhou, *Corros. Sci.* 185 (2021) 109408.
- [32] D. Abdelaziz, A. Hefnawy, E. Al-Wakeel, A. El-Fallal, I.M. El-Sherbiny, *J. Adv. Res.* 28 (2021) 51–62.
- [33] Y. Mu, S. Ma, P. Wei, Y. Wang, W. Jing, Y. Zhao, L. Zhang, J. Wu, B. Zhao, J. Deng, Z. Liu, *Adv. Funct. Mater.* (2021) 31.
- [34] D. Tie, F. Feyerabend, W.D. Muller, R. Schade, K. Liefeth, K.U. Kainer, R. Willumeit, *Eur. Cell Mater.* 25 (2013) 284–298.
- [35] M. Mohammadi-Zerankeshi, R. Alizadeh, S. Labbaf, *J. Mater. Res. Technol.* 22 (2023) 1677–1694.
- [36] Q. Wang, J. Chen, Z. Zhao, S. He, *Mat. Sci. Eng. A-Struct.* 528 (2010) 323–328.
- [37] L. Xiao, X. Chen, K. Wei, Y. Liu, D. Yin, Z. Hu, H. Zhou, Y. Zhu, *Scripta Mater.* 191 (2021) 219–224.
- [38] L.R. Xiao, X.F. Chen, Y. Cao, H. Zhou, X.L. Ma, D.D. Yin, B. Ye, X.D. Han, Y.T. Zhu, *Scripta Mater.* 177 (2020) 69–73.
- [39] D. Zhang, C. Liu, S. Jiang, Y. Gao, Y. Wan, Z. Chen, *Mat. Sci. Eng. A-Struct.* 856 (2022) 143990.
- [40] Z. Shu, C. Zhang, L. Yan, H. Lei, C. Peng, S. Liu, L. Fan, Y. Chu, *Int. J. Biol. Macromol.* 224 (2023) 1040–1051.
- [41] M. Mohammadi Zerankeshi, R. Alizadeh, E. Gerashi, M. Asadollahi, T.G. Langdon, *J. Magnes. Alloy* 10 (2022) 1737–1785.
- [42] D. Tie, F. Feyerabend, N. Hort, D. Hoeche, K. Kainer, R. Willumeit, W.D. Mueller, *Mater. Corros.* 65 (2014) 569–576.
- [43] Y. Jang, B. Collins, J. Sankar, Y. Yun, *Acta Biomater.* 9 (10) (2013) 8761–8770.
- [44] A. Shi, C. Zhu, S. Fu, R. Wang, G. Qin, D. Chen, E. Zhang, *Mater. Sci. Eng. C. Mater. Biol. Appl.* 109 (2020) 110548.
- [45] C.A. Shahed, F. Ahmad, E. Günister, F.M. Foudzi, S. Ali, K. Malik, W.S.W. Harun, *J. Magnes. Alloy* (2023), doi:10.1016/j.jma.2023.08.018.
- [46] M. Chen, L. Yang, L. Zhang, Y. Han, Z. Lu, G. Qin, E. Zhang, *Mater. Sci. Eng. C. Mater. Biol. Appl.* 75 (2017) 906–917.
- [47] Z. Zhang, J. Hu, Z. Xu, H. Huang, S. Yin, Y. Ma, J. Wei, Q. Yu, *Corros. Sci.* 198 (2022) 110107.
- [48] I. Sondi, B. Salopek-Sondi, *J. Colloid. Interface Sci.* 275 (2004) 177–182.
- [49] X. Chatzistavrou, J.C. Fenno, D. Faulk, S. Badylak, T. Kasuga, A.R. Boccaccini, P. Papagerakis, *Acta Biomater.* 10 (2014) 3723–3732.
- [50] J.L. Wang, J.K. Xu, C. Hopkins, D.H. Chow, L. Qin, *Adv. Sci.* 7 (2020) 1902443.
- [51] N. Wang, S. Yang, H. Shi, Y. Song, H. Sun, Q. Wang, L. Tan, S. Guo, *J. Magnes. Alloy* 10 (2022) 3327–3353.
- [52] X. Zhao, S. Wang, F. Wang, Y. Zhu, R. Gu, F. Yang, Y. Xu, D. Xia, Y. Liu, *J. Magnes. Alloy* (2022), doi:10.1016/j.jma.2022.07.002.
- [53] C.C. Hung, A. Chaya, K. Liu, K. Verdellis, C. Sfeir, *Acta Biomater.* 98 (2019) 246–255.
- [54] Y. Luo, H. Liu, Y. Zhang, Y. Liu, S. Liu, X. Liu, E. Luo, *Biomater. Sci.* 11 (2023) 7268–7295.
- [55] Y. Zhao, H. Cao, H. Qin, T. Cheng, S. Qian, M. Cheng, X. Peng, J. Wang, Y. Zhang, G. Jin, X. Zhang, X. Liu, P.K. Chu, *ACS. Appl. Mater. Interfaces* 7 (2015) 17826–17836.
- [56] S. Yang, L. Liang, L. Liu, Y. Yin, Y. Liu, G. Lei, K. Zhou, Q. Huang, H. Wu, *Mater. Sci. Eng. C. Mater. Biol. Appl.* 119 (2021) 111399.